Observation of Flake Graphite Nucleation and Growth in Gray Iron through Interrupted Solidification and Inclusion Analysis

Chandler Liggett, Mingzhi Xu, Jingjing Qing
Georgia Southern University, Statesboro, Georgia, USA

ABSTRACT

The solidification and cooling of a hypoeutectic gray cast iron was interrupted at various stages by quenching the samples using custom-made quartz molds in an iced brine. Microstructure evolution of the gray iron samples was interrupted and retained by quenching. A scanning electron microscope equipped with energy dispersive X-ray spectrometry (SEM-EDX) and Automated Feature Analysis Software was used to characterize the flake graphite and non-metallic inclusions. Based on the area and perimeter information obtained, length and thickness of flake graphite in various stages of solidification and cooling were achieved. Growth rates of type A graphite along the prismatic and basal directions during eutectic reaction were determined as 1.4 μm/s and 0.02 μm/s respectively. Inclusion analysis indicated the significant role of manganese containing sulfide and oxysulfide inclusions on nucleating graphite in gray iron.

Keywords: gray iron, interrupted solidification, flake graphite growth, growth rate, nuclei of flake graphite, evolutions

INTRODUCTION

Gray cast irons are widely used in combustion engine cylinder blocks, pump housing, machinery bases, valves and disc brake rotors, due to high stiffness, thermal conductivity, and vibration dampening properties. Typical gray irons contain 3-4 wt.% of carbon and 6-15 vol.% of graphite. Graphite in gray iron takes a three-dimensional flake morphology. The graphite flakes precipitate out from the liquid during the metal solidification process as a primary phase (forms Type C flake graphite) or sometimes as a product of Fe-C stable eutectic reaction. The size, distribution and volume percent of these graphite flakes as well as the matrix microstructure play important roles in controlling the mechanical and thermo-physical properties of gray cast iron.[1-3] The flake graphite formation during solidification can be divided as nucleation and growth processes.[4-7]

Type A flake graphite is generally desired in the gray iron microstructure. The addition of an inoculant in gray irons promotes the heterogeneous nucleation of flake graphite. Previous research has shown (Mn,X)S and Mn-O-S are linked to the nucleation of Type A flake graphite in gray irons. Riposan indicated that flake graphite nucleation happens on the complex (Mn,X)S and oxysulfide of Mn with inoculating elements (Ca, Sr, etc.), which were formed on top of early formed oxides of strong deoxidizing elements like Al and Zr.[8-10] Other studies also revealed the nuclei of flake graphite was Mn containing sulfides with oxide (normally with Al and Ca) cores.[5,11,12] The role of sulfides of rare earth on improving flake graphite nucleation were also reported.[11,13-15] These sulfide compounds have low crystallographic disregistry with graphite so they can serve as heterogenous nuclei for graphite.[4] Therefore, a sufficient amount of sulfur and oxygen are needed to ensure the formation of heterogeneous nuclei for flake graphite in the gray irons.

Figure 1 is a schematic projection of the {0001} basal planes of 2H graphite along the <0001> *c*-directions, and variations of the prismatic directions are demonstrated.[7] The 2H graphite is the most common form of graphite in nature. The broad faces of the flake graphite consist of primarily basal planes. The edges of the flake graphite are made of prismatic planes. After flake graphite nucleation, the graphite may grow along prismatic directions or normal to the basal plane. The growth in the *c*-direction will thicken a graphite flake, while the graphite flake becomes longer and wider due to the growth along the prismatic directions. Figure 2 is a schematic showing the growth of flake graphite along the *c*-direction and prismatic directions. In theory, if the graphite lattice contains no crystallographic defects or interruptions, growth of graphite will lead to a perfectly straight and flat graphite sheet. However, bending, rotating, and branching of lattice are common in the flake graphite, which is attributed to the presence of crystallographic defects (e.g., tilt boundaries, twin boundaries, and rotational stacking faults) in the graphite lattice structure.[7] Alloy elements may affect the occurrence frequency of crystallographic defects in the graphite, and thus leading to different graphite morphology.

The nucleation of flake graphite has been well studied in the past, however, growth of flake graphite in gray iron has not received as much attention. Additionally, statistical studies on the graphite flakes sizes and non-metallic inclusion are lacking. In this work, the authors utilized quenching samplers to “freeze” the graphite morphologies and non-metallic inclusions during different solidification stages. Statistical analyses on the graphite size distribution and inclusions were performed.

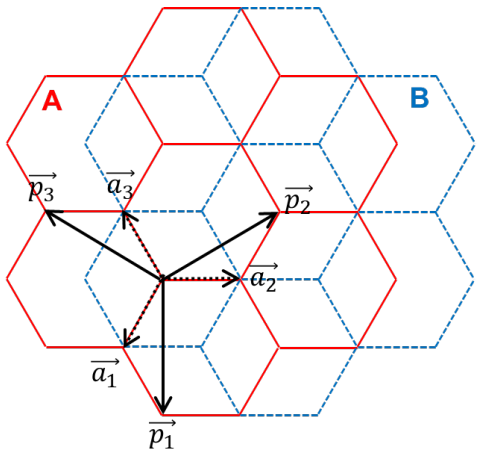

Figure 1. Schematic showing the stacking of {0001} basal planes in a 2H graphite (ABABAB…stacking sequence), with the variations of prismatic directions.

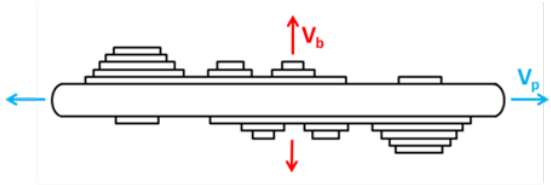

Figure 2. A schematic illustrating the flake graphite growth.[16]

EXPERIMENTAL

MOLD PREPARATION

A tubular mold made of quartz can withstand the high temperatures needed to contain liquid iron while its thin wall provides a spontaneous quench response. A 10 mm (0.39 in.) ID quartz tubing with 1 mm wall thickness was used to construct the mold. Sections of ~150 mm (5.9 in.) length were cut from the quartz tube, and one end was fused to form a test tube shape. Two holes of approximately 6 mm (0.24 in.) in diameter were blown on the side of quartz tube while heating the target location with high temperature flame. These holes served as metal inlet and air vent when sampling the molten metal. A smaller diameter quartz tube with fused end was inserted in the 10 mm (0.39 in.) quartz tube to house a thermocouple assembly, serving as a shield for the thermocouple tip.

The quartz tubes were assembled using silica investment shell slurry. Successive layers of ceramic slurry were added to build up the strength to hold the smaller tube in the larger quartz tube. A schematic of the quartz tube mold assembly with thermocouple is shown in Figure 3. A K-type thermocouple was inserted into mold and secured with ceramic slurry. A steel handle was also attached to the mold using ceramic slurry. Finally, thermocouple extension wire was attached to the thermocouple, and wrapped around the steel handling rod.

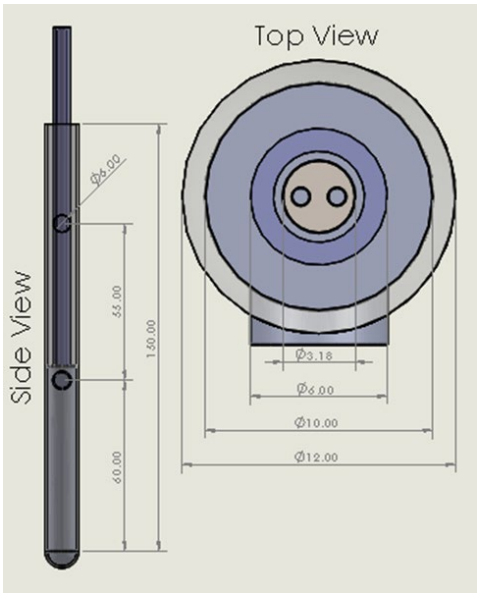

Figure 3. Schematic of the mold assembly with detailed dimensions (mm).

ALLOY SELECTION AND DEVELOPMENT

A hypoeutectic composition of gray iron was selected for the present study from a typical Class-30 gray iron composition: 1.8 wt.% Si and 3.4 wt.% C, which has a carbon equivalent (C.E.) of 4.0 wt.%. 0.6 wt.% Mn. Sulfur was intentionally kept low in this study to lower the count of heterogeneous nucleation sites and improve the visibility of evolutions for graphite flakes and non-metallic inclusions during solidification. The composition for the gray iron used in this study is listed in Table 1. The C and S were measured with a combustion analyzer, and the remaining elements were measured with an optical emission spectrometer (OES).

Table 1. Gray Iron Composition Used in Experiment

	C	Si	Mn	S	Cu
Wt.%	3.41	1.81	0.62	0.0060	0.02

MELT PREPARATION AND PROCEDURE

Charge materials as listed in Table 2 were used to produce the gray iron of a targeted chemistry. The charge materials were melted in an induction furnace in air. The metal was heated to 1500C (2732F) and held for 15 minutes to reach equilibrium oxygen and nitrogen in the melt. The inoculant was placed in the bottom of the ladle and the melt was de-slagged and tapped into the ladle. The inoculant addition rate was 0.3 % of the total weight, which is higher than the regular 0.15 wt.%, to ensure good inoculation of graphite in the thin specimen. Composition of the inoculant used is listed in Table 3. A chemistry sample was taken from the ladle, with the composition shown in Table 1.

Table 2. Charge Table Developed for Experiment

Materials	Weight (kg)	Weight (lbs.)
Pig Iron	22.00	48.40
Steel scrap	4.5	9.90
Fe75Si	0.530	1.17
FeMn	0.085	0.19
Graphite	0	0
Inoculant	0.08135	0.18
Total	**27.20**	**59.83**

Table 3. Composition of Inoculant used in Experiment

	Al	Ba	Ca	Si	Fe
wt.%	0.863	1.918	0.994	71.1	Bal.

A data acquisition (DAQ) system was connected to the K-type thermocouples in the mold assemblies to collect the temperature data of gray iron samples during solidification and cooling. The DAQ unit was configured to sample data at 0.5 second intervals. To take the samples, quartz mold assemblies were immersed in the molten iron at ~1300C (2372F) until molds were filled with iron. Six sets of mold assemblies were used to take samples from the liquid metal simultaneously but they were subjected to quenching at different stages of solidification and cooling. The immediate quench sample was withdrawn from the ladle and instantly plunged into the 5% iced brine after ~1 second. The other five samples were kept in the "nests" stuffed with an insulation blanket for retaining the heat and allowing consistent cooling rates across the multiple samples. Time was tracked once the mold assemblies were withdrawn from the ladle. After different holding times in the insulation nest, four samples were sequentially quenched in the iced brine. The holding times used were 30, 50, 70 and 80 seconds. The remaining sample was kept in the insulation blanket until cooled, and this sample was the unquenched sample.

MICROSCOPIC ANALYSIS

Samples were sectioned ~2.5 mm (0.1 in.) below the thermocouple tip location using a slow speed saw and were mounted in Bakelite. These samples were polished following a standard metallographic procedure and the finishing step used 0.3 µm (1.2e-5 in.) diamond paste. An optical microscope was used to capture the unetched microstructure.

A large population of graphite particles and non-metallic inclusions were characterized with an SEM/EDX and Automated Feature Analysis (AFA) Software. SEM-AFA operates by searching through a designated area in the sample automatically and detecting features of interest based on defined brightness and contrast threshold while the sample is imaged with a backscattered electron (BSE) detector, as demonstrated in Figure 4 (a) and (b). Once a feature of interest was detected when the threshold rule was satisfied, automated image analysis of the feature generated geometric information and EDX analysis of the feature produced chemical information. Classification rules can be applied to classify the feature based on its composition or geometry. This SEM-AFS algorithm allows statistical analysis of thousands of features of interest.

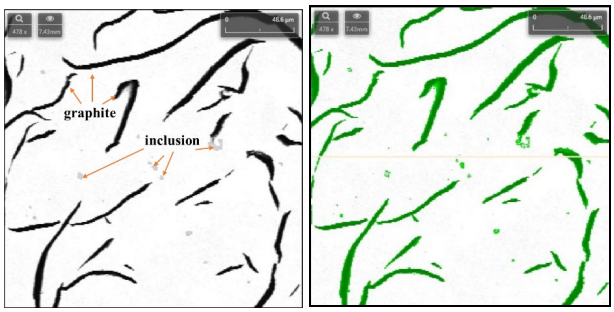

(a) (b)

Figure 4. (a) Backscattered electron image of gray iron containing flake graphite and inclusions in the matrix. (b) Demonstrates the detection (marked in green) of graphite and inclusions based on brightness and contrast threshold where darker phases were selected.

RESULTS AND DISCUSSION

COOLING CURVE ANALYSIS

Cooling curves of the six gray iron samples are plotted and shown in Figure 5 for comparison.

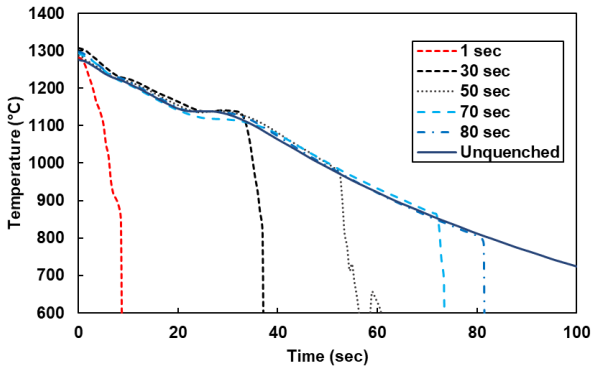

Figure 5. Recorded cooling curves of six samples for comparison.

First derivatives of the cooling curves were calculated using the temperature data of the unquenched sample, as shown in Figure 6. As demonstrated in a comprehensive study by Stan et al., the first derivative of the cooling curve can be plotted and overlaid onto the cooling curve to indicate the occurrence of phase transformations or reactions during solidification.[17] The first peak on the first

derivative curve in Figure 6 corresponds to the liquidus temperature (T_L) of the gray iron. The onset point at which eutectic solidification begins is indicated by the local minimum of the 1st derivative, which is labeled as T_E start. Lastly, the end of solidification (T_S) occurs at the second local minimum of the 1st derivative curve. The cooling curve obtained from the unquenched sample was used to determine the liquidus, eutectic start, and solidus temperatures for the gray iron selected, and the values are provided in Table 4. The different times corresponding to these critical temperatures are also listed in Table 4. The solidification stage for each quenched sample was determined based on the analysis of its individual cooling curve relative to that of the unquenched sample. It can be seen from Figure 5 that (1) 1-sec sample was quenched prior to the liquidus reaction from fully liquid state, (2) 30-sec sample was quenched during the eutectic reaction, and (3) 50-sec., 70-sec. and 80-sec. samples were all quenched after the completion of solidification.

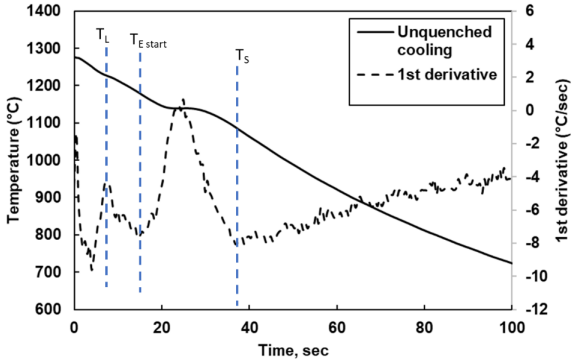

Figure 6. Cooling curve analysis with 1st derivative comparison.

Table 4. Critical Temperatures During Solidification of Gray Iron in Study

	Temperature (C)	Temperature (F)	Recorded Time (*sec*)
Liquidus T_L	1224.0	2235.2	8.0
Eutectic Start T_E start	1179.0	2154.2	15.0
Solidus T_S	1084.0	1983.2	37.4

MICROSTRUCTURAL ANALYSIS

Microstructural analysis was performed on the cross section at 2.5 mm (0.1 in.) location below the thermocouple tip. Micrographs for the six iron samples in the unetched condition are shown in Figure 7. Based on the microstructure from the unquenched sample (Figure 7f) and samples quenched after solidification was completed (50-sec, 70-sec and 80-sec, Figure 7c-e), the inoculation was effective to produce Type A flake graphite. Formation of Type D & E flake graphite in the 1-sec and 30-sec samples was due to fast cooling during quenching, as shown in Figure 7a-b.

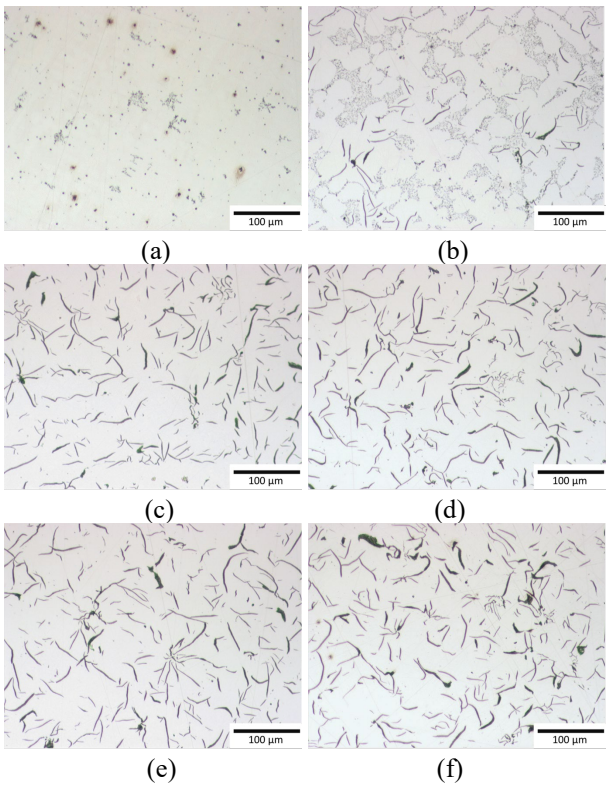

Figure 7. Unetched microstructures of 1-sec. sample (a), 30-sec. quenched sample (b), 50 sec. quenched sample (c), 70-sec. quenched sample (d), 80-sec. quenched sample (e), and unquenched sample (f).

While analyzing the data generated from SEM-AFA scans, a filter based on the area of individual graphite particles (≥25 µm^2) was applied to exclude the type D&E flake graphite thus, only Type A flake graphite was characterized. It can be seen in Figure 7a that 1-sec. sample has no Type-A flake graphite, so the flake graphite dimension was not analyzed for this sample. Perimeter (p) and area (A) of each individual graphite feature were populated after SEM-AFA analysis. The average length (l) and thickness (t) of a given graphite flake can be estimated using the following equations:

$$l = p \times 0.5$$

$$t = A / l = 2 \times A / p$$

It is worth noting that any 2-D metallographic analysis technique inspects a cross-section of a 3-D volume. Because of the complex nature of the interconnected type A flake graphite network, the SEM-AFA results based on a 2-D cross-section only present the length of 3-D graphite network after being randomly sectioned.

Table 5. Average Graphite Thickness & 10% Longest Graphite Average Length of Samples Based on SEM-AFA Analysis

Quench Time, *sec.*	Growth Time in Eutectic, *sec.*	Growth Time after Eutectic, *sec.*	Total Graphite Captured	Average Graphite Thickness, *um*	10% Longest Graphite Average Length, *um*
30	15.0	0.0	196	1.13	97.4
50	22.4	12.6	4,840	1.45	118.8
70	22.4	32.6	4,840	1.30	116.3
80	22.4	42.6	4,952	1.32	120.7
Unquenched	22.4	100+	5,458	1.27	111.9

For example, a shorter flake graphite appearing in 2-D microstructure may be an edge of a large flake graphite in 3-D that is partially sectioned. As a result, instead of using the average length measured on the 2-D cross-section, the 10% longest graphite flakes observed in 2-D were selected to better represent the actual graphite length in 3-D. Graphite growth time in all samples (in relative to the beginning of sampling), average graphite thickness and 10% longest graphite average length, are listed in Table 5.

It can be seen from Table 5 that graphite lengthening and thickening occurred during eutectic solidification, due to the fast carbon diffusion when liquid was present. After solidification was complete, graphite thickness and length remained almost constant. Average half-length of 10% longest graphite and average thickness of all graphite are plotted against growth time during eutectic solidification as shown in Figure 8. Similar to Amini's observation on Type C graphite in a Ni-C alloy system, the graphite growth rate is relatively high at the beginning of the growth, because the driving force for interface migration is high due to large amount of supersaturation and availability of carbon atoms.[16] After the initial growth period, the graphite flake growth rates along prismatic and basal planes are steady, and the plot of graphite dimensions versus time should have constant slopes.

From Figure 8, the graphite growth rate (V_p) along the prismatic direction was found to be two magnitudes faster when comparing with growth rate along the c-direction (V_b) (1.44 µm/sec vs 0.02 µm/sec). In addition, the prismatic growth rate determined in this study is similar to Amini's finding on Type C flake graphite[16] (1.44 µm/sec vs 1.80 µm/sec). Growth rate along the c-direction was found much lower than Amini's result (0.02 µm/sec vs. 0.10 µm/sec).[16] This possibly indicated Type A flake graphite had a slower growth rate along the c-direction normal to the basal planes compared with Type C graphite. Indeed, the Type-A flake graphite is normally thinner than the Type-C flake graphite in the gray iron, which may be attributed to the difference in growth rate along the thickness direction, i.e., c-direction.

INCLUSION EVOLUTION

Non-metallic inclusions in all gray iron samples were also analyzed using SEM-AFA. The number density of Mn-containing inclusions as well as other oxides and nitrides inclusions are shown in Figure 9 as a function of quench time. At low sulfur levels in gray iron, which is the case for the present study, quenching the liquid metal promoted the formation of Mn-O-S inclusions, and the number density for these oxy-sulfide inclusions were measured at 724/mm^2 (in 1-sec. quenched sample). Detailed EDX analyses on these Mn-O-S inclusions did not show a concentration of Al so they were not complex inclusions with Al_2O_3.

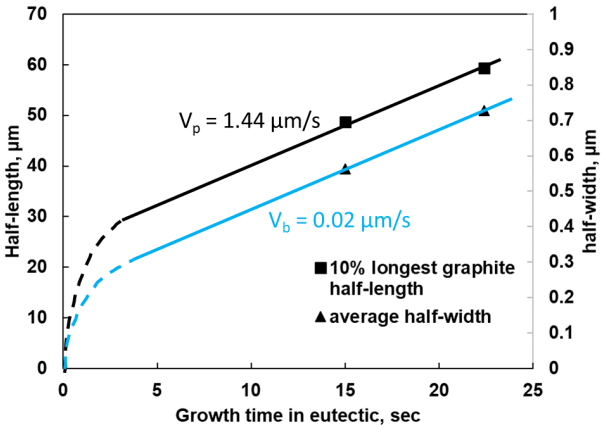

Figure 8. Half-length and half-width of flake graphite as a function of growth time during the eutectic reaction of the gray iron sample, and growth rates along prismatic direction and c-directions were determined based on the slope of the curves.

As shown in Figure 9, a decrease in Mn oxysulfide number density was observed during eutectic solidification. Recent research performed by Riposan et al. (2020) found an oxide layer on the MnS which promoted nucleation of flake graphite in gray iron.[4] In this research, these Mn oxysulfide inclusions were considered as the nuclei for graphite. Graphite flakes formed may partially or entirely cover the Mn oxysulfide inclusions in 3-D, making it undetectable in 2-D analysis. In the meantime, an increase in the number density of other

oxide inclusions (SiO_2, Al_2O_3, Al_2SiO_5) was observed during graphite formation. Compositions of Mn oxysulfide in samples quenched at different stages of solidification are shown in the ternary diagrams in Figure 10. When the sample was quenched before the start of solidification, because of the low sulfur content in the liquid metal, the oxysulfide inclusions formed had higher oxygen content (Figure 10a). Thermodynamic calculations using FactSage 8.2 and FS-Steel Database indicated that MnS formed at around 1154C (2109F) during an equilibrium solidification, shortly after the start of graphite formation during eutectic solidification. As solidification began, MnS inclusions became more stable, and the oxysulfide inclusion contained higher sulfur (Figure 10b). Such change could release more oxygen that was tied up in Mn-O-S inclusions, which formed more other oxide inclusions. When solidification completed, most of the sulfur was spent in forming Mn-O-S and MnS inclusions, thus these oxysulfide inclusions had a higher S content as shown in Figure 10c.

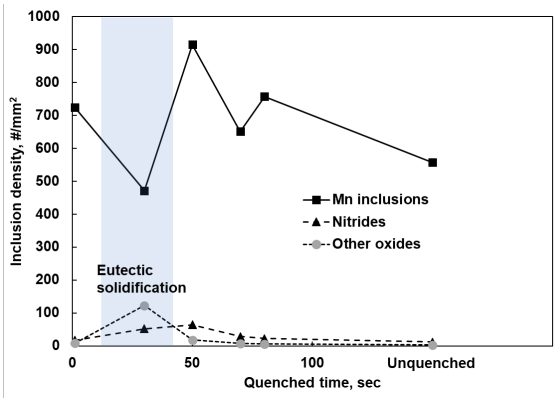

Figure 9. Inclusion number density at various stages of solidification; shaded area highlights the duration of eutectic solidification.

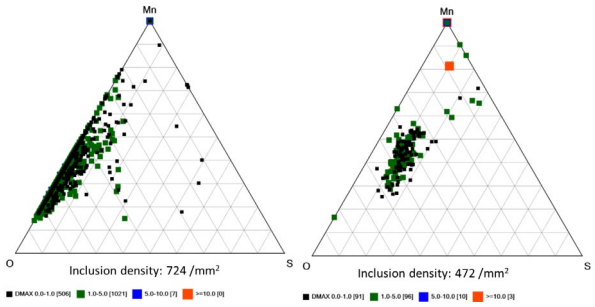

(a) (b)

Figure 10. Ternary diagrams showing composition and number density evolutions of Mn-O-S inclusions during gray iron solidification at specific moments: view (a) direct quench from liquid, (b) during eutectic solidification, view (c) continued next column.

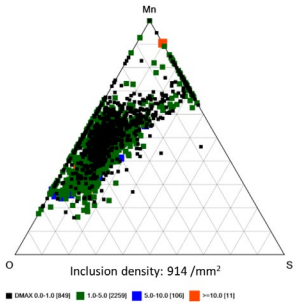

(c)

Figure 10(c) continued…Ternary diagrams showing composition and number density evolutions of Mn-O-S inclusions during gray iron solidification at specific moments: (a) direct quench from liquid, (b) during eutectic solidification,(in previous column) and (c) 12 seconds after solidification was completed.

CONCLUSIONS

Graphite nucleation and growth in gray iron was studied using an interrupted solidification experiment. Graphite and non-metallic inclusions in the quenched gray iron samples retained at various stages of solidification were characterized using SEM-AFA-EDX. Type A flake graphite growth rate during eutectic solidification of a hypoeutectic gray iron was measured as 1.4 µm/sec along the prismatic direction and 0.02 µm/sec normal to the basal planes. Inclusion analysis showed the dominating role of Mn-O-S inclusion on nucleating graphite in gray iron.

REFERENCES

1. Xu, W., Ferry, M. & Wang, Y., “Influence of alloying elements on as-cast microstructure and strength of gray iron,” *Mater. Sci. Eng. A*, 390, 326–333 (2005).
2. Muhmond, H.M. & Fredriksson, H., “Relationship between inoculants and the morphologies of MnS and graphite in gray cast iron,” *Metallurgical and Materials Transactions B: Process Metallurgy and Materials Processing Science,* 44, 283–298 (2013).
3. Rivera, G.L., Boeri, R.E. & Sikora, J.A., “Graphite nucleation sites in commercial grey cast irons,” *Mater Today Proc,* 45, 4091–4095 (2020).
5. Sommerfeld, A. & Tonn, B., “Theory of graphite nucleation in lamellar graphite cast iron,” *International Journal of Metalcasting,* 3, 39–47 (2009).
6. Double, D.D. & Hellawell, A., “The nucleation and growth of graphite—the modification of cast iron,” *Acta Metallurgica et Materialia*, 43, 2435–2442 (1995).

7. Qing, J., Lekakh, S., Xu, M. & Field, D., “Formation of Complex Nuclei in Graphite Nodules of Cast Iron,” *Carbon* (NY) 171, 276–288 (2021).
8. Chisamera, M., Riposan, I., Stan, S., White, D. & Grasmo, G., “Graphite nucleation control in grey cast iron,” *International Journal of Cast Metals Research* 21, 39–44 (2008).
9. Riposan, I., Chisamera, M., Stan, S., Hartung, C. & White, D., “Three-stage model for nucleation of graphite in grey cast iron,” *Materials Science and Technology*, 26, 1439–1447 (2010).
10. Riposan, I., Chisamera, M., Stan, S. & Skaland, T., “Graphite nucleant (microinclusion) characterization in Ca/Sr inoculated grey irons,” 567 16, 105–111 (2016).
11. Moumeni, E., Stefanescu, D.M., Tiedje, N.S., Larrañaga, P. & Hattel, J.H., “Investigation on the effect of sulfur and titanium on the microstructure of lamellar graphite iron.” *Metall Mater Trans A Phys Metall Mater Sci,* 44, 5134–5146 (2013).
12. Jianzhong, L., “Heterogeneous nuclei of graphite in grey cast iron,” *Materials Science and Technology*, 4, 740–744 (1988).
13. Nakae, H. & Igarashi, Y., “Influence of sulfur on heterogeneous nucleus of spheroidal graphite,” *Mater Trans,* 43, 2826–2831 (2002).
14. Adjizian, J.J., Latham, C.D., Öberg, S., Briddon, P. R. & Heggie, M.I., “DFT study of the chemistry of sulfur in graphite, including interactions with defects, edges and folds,” *Carbon* (NY) 62, 256–262 (2013).
15. Hiratsuka, S., Horie, H., Kowata, T., Lee, S.H. & Choi, C.O., “Effect of rare earth elements and sulfur on microstructure and chilling tendency in flake graphite cast iron,” *International Journal of Cast Metals Research,* 16, 113–117 (2003).
16. Amini, S. & Abbaschian, R., “Nucleation and growth kinetics of graphene layers from a molten phase,” *Carbon* (NY) 51, 110–123 (2013).
17. Stan, S., Chisamera, M., Riposan, I. & Barstow, M., “Application of thermal analysis to monitor the quality of hypoeutectic cast irons during solidification in sand and metal moulds,” *J Therm Anal Calorim*, 110, 1185–1192 (2012).